IOP Publishing Phys. Med. Biol. 70 (2025) 125004 https://doi.org/10.1088/1361-6560/addf0d

Physics in Medicine & Biology

IPEM Institute of Physics and Engineering in Medicine

PAPER

RECEIVED
4 March 2025

REVISED
15 May 2025

ACCEPTED FOR PUBLICATION
30 May 2025

PUBLISHED
10 June 2025

Modeling prompt gamma (PG) emission, detection and imaging in real patient anatomy using a novel Compton camera for dose verification in proton therapy

V R Sharma[1,*], Z Jiang[2], S Mossahebi[3], E Shakeri[4], A Chalise[1], M K Gobbert[4], S W Peterson[5], J C Polf[6,*] and L Ren[1,*]

[1] Department of Radiation Oncology, School of Medicine, University of Maryland, Baltimore, MD 21201, United States of America
[2] Department of Radiation Oncology, Stanford University, Stanford, CA 94304, United States of America
[3] Maryland Proton Treatment Center, Baltimore, MD, United States of America
[4] Department of Mathematics and Statistics, University of Maryland Baltimore County, Baltimore, MD, United States of America
[5] Department of Physics, University of Cape Town, Rondebosch 7700, South Africa
[6] M3D, Ann Arbor, MI 48108, United States of America
[*] Authors to whom any correspondence should be addressed.

E-mail: vsharma@som.umaryland.edu, jpolf@m3dimaging.com and lren@som.umaryland.edu

Keywords: Monte Carlo simulations, prompt gamma imaging, Compton cameras, kernel weighted back projection, proton therapy

Abstract

Objective. Prompt gamma (PG) imaging is a promising modality for proton dose verification. Currently, there is a lack of effective tools to investigate the entire PG imaging process in patient anatomy, from PG emission to camera detection and image reconstruction, to evaluate and optimize its efficacy for dose verification in proton therapy. *Approach*. To address this gap, we developed a Monte-Carlo package, POLARIS J Monte Carlo (PJ-MC), that simulates the entire PG emission and imaging workflow in patient anatomy. We utilized Geant4 classes and G4-ancillary tools, employing the DCMTK external tool with G4PhantomParameterisation to convert patient CT data into voxelized geometries. Proton beams were modeled based on medical physics commissioning data. A novel two-stage POLARIS-J3 Compton-Camera was simulated under the patient couch for recording total, double, and triple scattered PG signals. Proton maximum range calculations from the PJ-MC are compared with dose calculations from a clinical treatment planning system. The detected PG signals data in the simulation were used to reconstruct PG images using Kernel- Weighted-
Back-Projection algorithm. *Main results*. Analysis of gamma energy distribution showed a decay pattern with clear emission lines from nuclear reactions involving oxygen, carbon, nitrogen, and calcium. Neutron-induced reactions contribute significantly less-by an order of magnitude-compared to proton-induced reactions in various tissues. Mean absolute percentage error analysis showed that PG range verification was more stable when considering the range at 80% or 50% of D_{max}, as opposed to the range at the D_{max}, where energy gating slightly improves accuracy but may reduce localization due to photon loss. Results showed that patient anatomy can impact the location of hot spot in the PG images, affecting its accuracy for localizing Bragg peak. *Significance*. In summary, our simulation package provides additional insights into PG emission and imaging in patient anatomy and serves as a robust tool for evaluating and optimizing PG imaging, enhancing its precision for dose verification in proton therapy.

1. Introduction

In clinical proton therapy, one of the biggest advantages is the sharp dose drop-off at Bragg peak located at the end of the proton beam (Hu *et al* 2018, Reaz *et al* 2022), which allows radiation to be deposited at the tumor region while sparing healthy tissues beyond the tumor depth. However, this precision is often affected

by uncertainties in the proton range (Paganetti 2012, Lomax 2019). These uncertainties arise due to inaccuracies in proton dose calculation based on CT, anatomical changes during treatment, and variations in patient positioning. To compensate for this uncertainty, safety margins of $\pm 3.5\%$ (overshooting and undershooting by 3.5%, resp.) are commonly added to the original target volume (Nishioka *et al* 2022). While this ensures the tumor receives the full radiation dose, it also increases the exposure of healthy tissues to unnecessary radiation, which defeats the purpose of using proton therapy for tissue sparing.

To overcome these challenges, researchers have focused on developing real-time monitoring tools to verify proton beam delivery (Bom *et al* 2011, Krimmer *et al* 2018, Parodi and Polf 2018, Jacquet *et al* 2021, Yap *et al* 2021, Martins *et al* 2024). These tools help reduce safety margins, making treatment more precise and improving patient outcomes. One of the most promising approaches is prompt gamma (PG) imaging, which detects gamma rays produced when protons interact with tissues, offering immediate feedback on beam positioning. This allows for potential adjustments during treatment, improving accuracy and reducing unnecessary radiation exposure.

The first clinical application of a PG-based *in vivo* proton range verification system has been reported (Richter *et al* 2016, Berthold *et al* 2021), marking an important milestone in the field. This pioneering study demonstrated that PG imaging could be used during clinical proton therapy to improve treatment accuracy by verifying the proton beam range in real-time.

The PG imaging system in that study used a knife-edge slit collimator, which projected the gamma-ray emission profile onto an array of 40 scintillation detectors arranged in two rows. These detectors were optimized to capture gamma rays within the 3–6 MeV energy range, allowing for spatially resolved gamma detection. While this setup enabled real-time monitoring of the proton beam's range, it had several limitations. The collimator's narrow field of view made it difficult to track the entire proton beam path, especially for large or complex tumors. Additionally, the slit design allowed only a small fraction of PG rays to reach the detector, requiring higher proton doses for reliable measurements, which may not be ideal for patient safety. Another challenge was that knife-edge slit collimators provide only one-dimensional (1D) gamma profiles, limiting their ability to reconstruct a full three-dimensional (3D) view of the gamma distribution during treatment.

These limitations highlight the need for more advanced PG imaging techniques in proton therapy. One promising approach is using Compton cameras (CC), such as cadmium zinc telluride (CZT)-based systems, which could improve imaging resolution and efficiency. Recently, Maggi *et al* (2020) developed a Monte Carlo (MC) plus Detector Effects model of the prototype Polaris-J3 (PJ3) CC, designed for PG imaging during proton treatment. Their study examined how increasing the number of data readout channels and reducing the charge collection and readout/reset deadtime within the onboard data acquisition electronics of the PJ3 affect the recorded data over the full range of clinical proton radiotherapy dose rates.

In another study, Panthi *et al* (2021) introduced a novel Kernel Weighted Back Projection (KWBP) algorithm to improve gamma image reconstruction in PJ3 CC. This algorithm uses a kernel density estimation method to back-project gamma-ray interaction data into a voxel-based image, reducing noise and improving image clarity. Their evaluation showed that this technique could estimate the maximum of the signal peak in water phantoms by 24 mm away from the dose fall off.

Despite the promise of this novel CC for 3D dose verification, previous simulation studies were carried out only in water or uniform phantoms (such as PMMA) rather than real patient anatomy (Moteabbed *et al* 2011, Polf *et al* 2013, Chen *et al* 2018, Hueso-González *et al* 2018, Fontana *et al* 2020). Currently, there is a lack of simulation tools that can simulate the entire PG imaging process in patient anatomy, from PG emission to camera detection and image reconstruction, to evaluate and optimize the efficacy of this PJ3 CC system for dose verification in proton therapy. To bridge this gap, we developed a Geant4 model named POLARIS J Monte Carlo (PJ-MC) that simulates imaging process in patient anatomy using the PJ3 CC, allowing us to investigate its efficacy for proton range or dose verification in various clinical settings.

Based on this new development, this study further evaluated gamma yield patterns per Monitor Unit (MU), emission counts based on tissue density, and detected PG signals in the format of double- and triple-stacked arrays by the CC. We analyzed multiple clinical scenarios in the prostate region under distinct conditions: (1) using a fixed energy layer while varying spot positions associated with different MUs, and (2) using a fixed MU while varying energy layers and spot positions. The proton dose maximum (D_{max}) was compared with the RayStation treatment planning system (TPS) to validate the accuracy and reliability of our approach. Additionally, we assessed the performance of the KWBP algorithm by using double and triple scattering gamma detection and applying a gated energy window for total PG signal detection and imaging.

The following sections describe the materials and methods used in this study, including the conversion of CT images into a voxel-based phantom, the experimental setup within the Geant4 framework, beam profiling data from the TPS, the relevant physics processes, and a brief overview of the KWBP algorithm. The results are then presented, followed by a discussion and conclusion summarizing key findings and their implications.

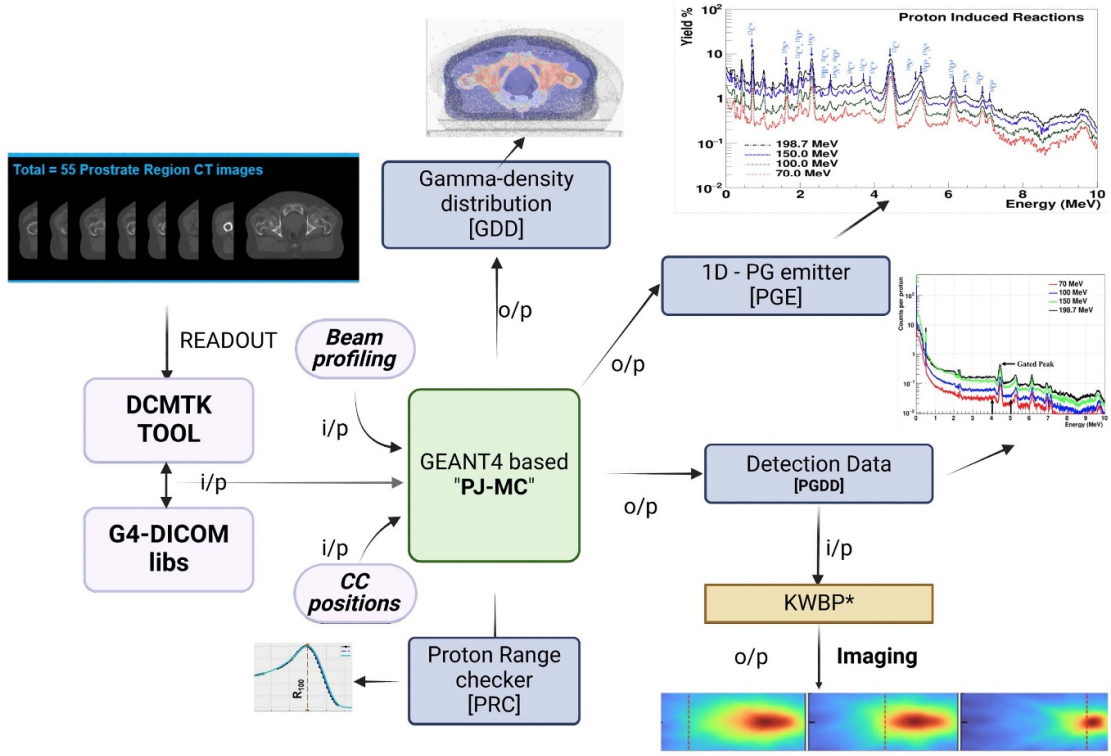

Figure 1. Workflow illustrating the simulation and analysis process for evaluating gamma hotspots using PJ-MC. The process involves CT image importation, data conversion, proton range checking, emission filtering, and gamma hotspot reconstruction with the *Kernel Weighted Back-Projection algorithm.

2. Material and methods

Geant4 is a powerful object-oriented toolkit designed to accurately simulate how particles interact with matter (Agostinelli *et al* 2003, Allison *et al* 2006, 2016). In this study, we developed a MC simulation package called PJ-MC, which incorporates various Geant4 classes along with a DICOM extension to efficiently handle CT image data using the DCMTK toolkit. The Geant4 framework was used to convert real patient CT images into a 2D array, storing material properties, densities, and voxel dimensions based on the selected compression level.

A workflow overview for simulating PG imaging process in patient anatomy is shown in figure 1. The process begins with importing CT images of a prostate cancer patient using the DCMTK software. The dataset consists of 55 CT slices, each with a resolution of 512 × 464 pixels and a spatial resolution of 0.97 × 0.97 × 3 mm^3. These CT images provide critical information about electron densities, derived from Hounsfield Unit (HU) values. To integrate this data into the Geant4 simulations, HU values are converted into material properties-including elemental composition and mass density-using the DCMTK toolkit and Geant4 DICOM libraries.

For the conversion of HU values, we employed Schneider's approach (Schneider *et al* 2000), which divides the HU scale (−1000 to 1600) into 24 distinct groups. Each group retains a consistent elemental composition and relative element weights, while the mass density is adjusted based on the specific HU value. This method ensures an accurate representation of tissue properties in the simulation, leading to a realistic model of the patient's anatomy.

The processed CT data serves as the input for PJ-MC, representing the patient-specific anatomical structure. The complete experimental workflow is shown in figure 2, detailing each step of the process. After selecting the proton localization, defining energy configurations, and positioning the PJ3-CC, the PJ-MC generates four key stacked data files in ROOT format (Brun and Rademakers 1997). These detection data files are then post-processed using the KWBP algorithm to reconstruct gamma hotspots, enabling verification of proton beam ranges at D_{max}. and dose delivery.

2.1. PJ-MC geometry setup

The experimental geometry in the MC model was designed based on TPS coordinates (Janson *et al* 2024), as shown in figure 2. The setup included a patient target phantom placed at the isocenter with coordinates

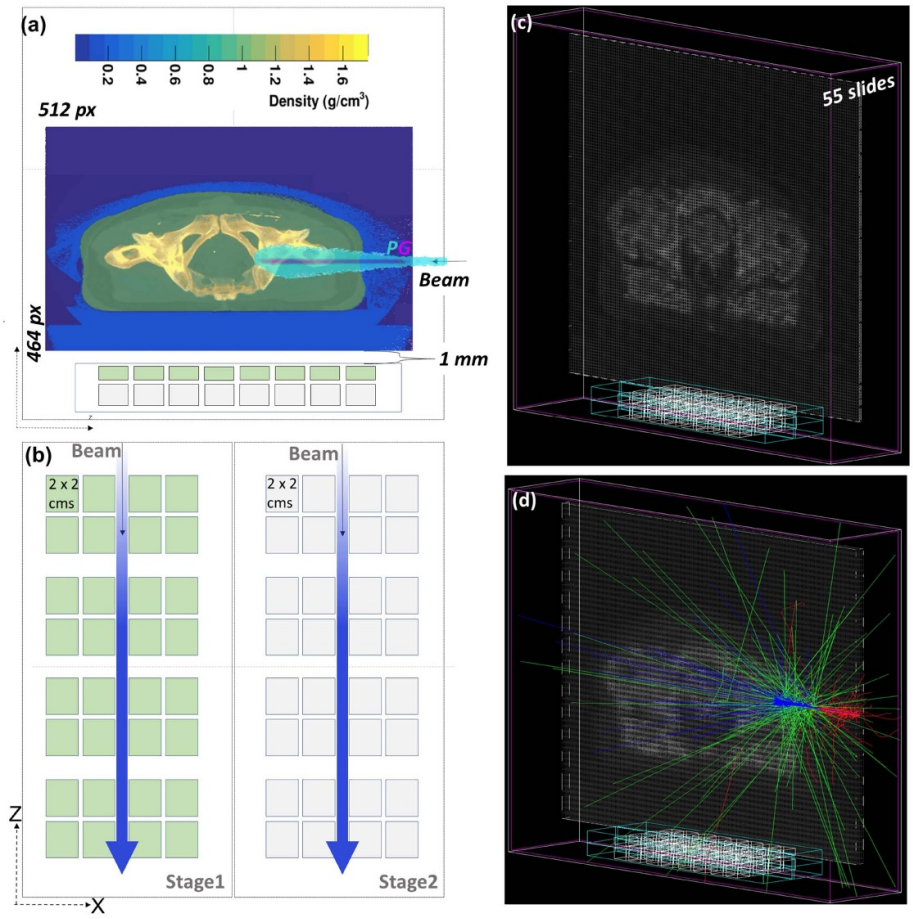

Figure 2. (a) Illustration of the experimental setup (X–Y plane) in Geant4. (b) View of the detection system on the ZX plane. (c)–(d) Snapshot taken from the QT window of Geant4 without and with the proton beam. (figure dimensions not to scale).

(13.8 mm, 12.6 mm, 0.5 mm). The Z-axis represents the beam's entrance direction, with the gantry rotated to 90°, allowing the beam to travel from the right to the left side of the patient. The Y-axis represents the anterior ($+Y$) and posterior ($-Y$) directions, while the X-axis corresponds to the head ($+X$) and feet ($-X$) directions, termed as HF and AP, respectively.

The original CT image size was 512 × 512 pixels in the YZ plane. However, 48 pixels were removed from the posterior region to make space for a detection unit beneath the patient couch. This helped to overcome a problem of overlapping geometries in the model. The patient?s final simulation dimensions were 512 pixels (Z-axis), 464 pixels (Y-axis), and 55 pixels (X-axis). The detection system consisted of two stages of CZT crystals placed below the patient couch, separated by a 1 mm air gap.

Figure 2(b) illustrates the two detection stages of CC. Stage 1 contains 32 CZT crystals, each measuring 2 cm × 1 cm × 2 cm, while Stage 2 consists of thicker CZT crystals measuring 2 cm × 1.5 cm × 2 cm. The Stage 1 detectors were positioned at −214.9 mm, and Stage 2 detectors were positioned at –232.9 mm from the target isocenter. The CZT-CC system detects PG signals using a counter method after each event.

Renderings of the modeled geometry are provided in figures 2(c) and (d), showing the setup using four CT slices. Figure 2(d) also shows particle tracks for 100 primary protons, where protons appear in blue, gammas in green, and electrons in red.

2.2. Beam data and physics models

The PJ-MC package uses proton pencil beam (PPB) parameters obtained from the Raystation V11B (Raysearch Laboratories, Stokholm Sweden) TPS. These parameters define the 2D Gaussian beam spot sizes (σ_x, σ_y) and the 1D Gaussian energy spread, characterized by an initial mean energy (E_0) and energy spread (ΔE). Since this study focuses on a single energy layer (198.7 MeV), only one set of beam spot sizes is considered with values of $\sigma_x = 4.016$ mm, $\sigma_y = 3.865$ mm using TPS data.

To achieve accurate particle tracking and secondary radiation modeling, the emstandard option-4 physics model in Geant4 was used. This model is designed for high-accuracy applications in electron, hadron, and ion tracking and utilizes the most precise standard and low-energy models available in Geant4.

Additionally, the following physics models were included to simulate secondary particle interactions and radiation processes:

G4DecayPhysics—Handles decay processes of unstable particles.
G4HadronElasticPhysics—Models elastic scattering of hadrons.
G4StoppingPhysics—Simulates the energy loss of stopping particles.
G4IonPhysics—Provides interactions of ions with matter.
G4NeutronTrackingCut—Applies cuts to improve neutron transport efficiency.
G4RadioactiveDecayPhysics—Simulates radioactive decay processes.
G4EmStandardPhysicsGS—An advanced electromagnetic model for accurate dose calculations.

These models have been extensively validated in previous proton therapy studies (Jeyasugiththan and Peterson 2015, Wrońska *et al* 2021), ensuring that the simulation reliably replicates proton beam interactions, secondary particle production, and radiation transport in a clinical environment.

2.3. Key features of the KWBP imaging algorithm

The KWBP algorithm, is a GPU-optimized method designed for image reconstruction of CC images. The KWBP algorithm reconstructs the spatial distribution of gamma sources by projecting half-cone surfaces, which are derived from double- or triple-scattered events, into a voxel-based 3D image space. The probability of gamma emissions is calculated for each voxel using the Epanechnikov kernel density estimation, which determines the minimum distance between the voxel center and the half-cone surface. This method improves reconstruction accuracy by focusing probability estimates around the most likely gamma emission origins.

To further enhance image quality and reduce noise, the algorithm employs a random shuffling technique. In this approach, cones are randomly shuffled and back-projected into the image space. The resulting image is then subtracted from the initial reconstruction, effectively suppressing artifacts and enhancing image clarity. For more details on the KWBP algorithm, readers can refer to Panthi *et al* (2021).

3. Results

The study examines the emission of PG signals resulting from proton and neutron inelastic interactions based on patient-specific data, along with their subsequent detection by the PJ3-CC and image reconstruction in distinct clinical scenarios. Initially, the energy layer was fixed at 198.7 MeV while three different proton beam spots were analyzed, each delivered with a different MU. Subsequently, another condition was simulated where three spots were delivered with a fixed MU, but varying energy layers and spot positions, all in accordance with the patient treatment plan generated by a ProBeam machine. The double- and triple-scattering events were recorded while excluding other interactions to better understand the overall imaging process within the KWBP framework. An effort was made to explore the impact of energy-gated windowing on gamma hotspot localization. The results presented in this section aim to provide a comprehensive understanding of PG emission behavior and the imaging process using the Polaris CC within patient anatomy, along with its implications for proton therapy verification.

3.1. Patient specific PG emission

Figure 3 presents the energy spectrum of PGs generated along the proton beam path within the patient. The spectrum displays distinct gamma peaks over a broad energy range, superimposed on an exponentially decreasing continuum. The most prominent peak appears at 4.44 MeV, primarily resulting from proton (or neutron) interactions with oxygen and carbon nuclei. These interactions produce excited Carbon-12 nuclei (^{12}C) via reactions such as ^{16}O(p, $x\gamma$)^{12}C* and ^{12}C(p, p'γ)^{12}C*. Other significant peaks at 5.18, 5.24, and 6.18 MeV correspond to de-excitations of oxygen-15 nuclei (^{15}O)*, while peaks at 5.27, 5.30, and 6.32 MeV arise from nitrogen-15 (^{15}N) de-excitations. Additionally, gamma lines at 6.13, 6.92, and 7.12 MeV are associated with inelastic interactions involving oxygen-16 nuclei (^{16}O)*. Lower-energy peaks are attributed to boron (^{10}B, ^{11}B), nitrogen (^{14}N, ^{15}N*), and carbon (^{11}C*) interactions. These findings are consistent with previous studies conducted using water (Zarifi *et al* 2017), solid water phantoms and PMMA, as well as simulations for head and neck regions (Paganetti 2012).

Furthermore, neutron-induced PGs contribute across the entire energy spectrum, with notable peaks between 0 and 7 MeV. While neutron interactions are weaker, they still play a role through capture and inelastic processes. For instance, the capture reaction ^{1}H(n, γ)^{2}H emits a 2.22 MeV gamma line, while inelastic interactions produce lines at 4.44 MeV corresponding to de-excitations of ^{12}C*. Approximately 27% of the 4.44 MeV peak in the total PG spectrum is due to neutron interactions, with smaller contributions at 5.30 MeV (≈19%) and 6.13 MeV (≈30%).

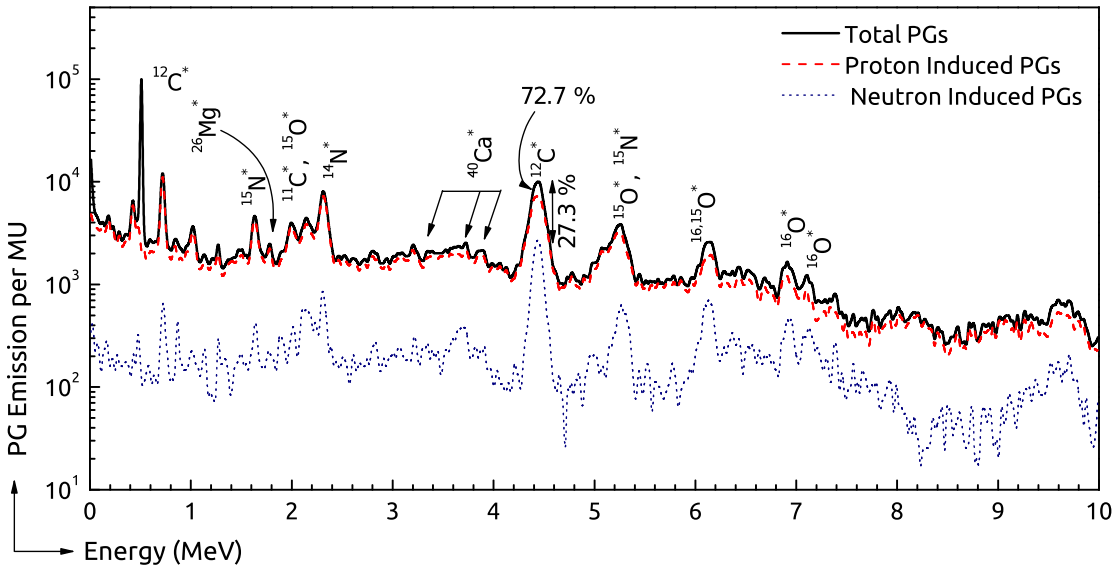

Figure 3. PG Emission spectra per MU for a single energy layer of 198.7 MeV as per treatment plan. The highlighted characteristic gamma emission lines correspond to interactions within the patient's anatomy with different elements.

An attempt has been made with a presentation of two-D histogram of PG emission specific to the prostate region in figure 4, highlighting how gamma emission behavior varies with tissue composition, particularly due to elemental concentrations. Figure 4 illustrates the categorization of PG origins from proton and neutron induced reactions and their simulated linear energy spectra into four tissue density regions (TDR) grouped as follows:

TDR1 : Density range: 0 to 0.8 g cm^{-3}, covering materials like air, fiber, cloth etc.
TDR2 : Density range: 0.8 to 1.125 g cm^{-3}, covering water-like tissues, soft tissues, etc.
TDR3 : Density range: 1.125 to 1.34 g cm^{-3}, covering muscular tissues.
TDR4 : Density range: 1.341 g cm^{-3} and above, covering bones or skeletal tissues.

As shown, the emission of PG signals (order of magnitude $\approx 10^3$) is maximized due to proton inelastic interactions with TDR2. In contrast, PG signal emission from neutron inelastic interactions with TDR2 is observed to be reduced by approximately one order of magnitude (see figure 4, right panel), with a peak at 4.44 MeV corresponding to the de-excitation of $^{12}C^*$. This behavior is consistent across other TDRs; however, a notable difference is observed in the two-dimensional histogram (top panels). Specifically, PG line emissions from neutrons are more scattered, generating signals from positions farther along the beam path. Given the lower order of magnitude of neutron-induced PG emissions, their impact on image reconstruction is expected to be minimal, as discussed in the next section. Nevertheless, classifying PG signals may be valuable from the fundamental physics perspective, as different nuclear reactions produce distinct characteristic gamma lines corresponding to interactions with specific elemental compositions. As such, an attempt has been made to normalize the energy spectra with energy bins and primary number of protons. As a representative case, proton-induced PG line at 0.718 MeV from the TDR2 observed to be minimum when comparing to other TDRs. This could be attributed to the different carbon concentrations in the tissue region, as discussed (Martins *et al* 2020). On the other hand, for neutron inelastic interactions, TDR4 was found to contribute relatively least yield to the final neutron-induced spectra (as shown in figure 3) when compared to other tissue regions. This suggests that the cumulative cross-section may play an important role during the de-excitation of $^{12}C^*$ nuclei shaping the observed PG emission. Since TDRs are made up of tissues with different densities (i.e. heterogeneous), a further step can be taken to classify each tissue type using HU ranges from patient-specific data, and assign appropriate material indexes. In Olsson *et al* (1989), Martins *et al* (2020), Wang *et al* (2022), the authors attempted an experimental approach using homogeneous media to quantify the presence of oxygen and carbon elements through PG emission analysis. This classification could be particularly useful in determining the relative contribution of different elements within a tissue, providing insights into the elemental composition and its role in PG imaging.

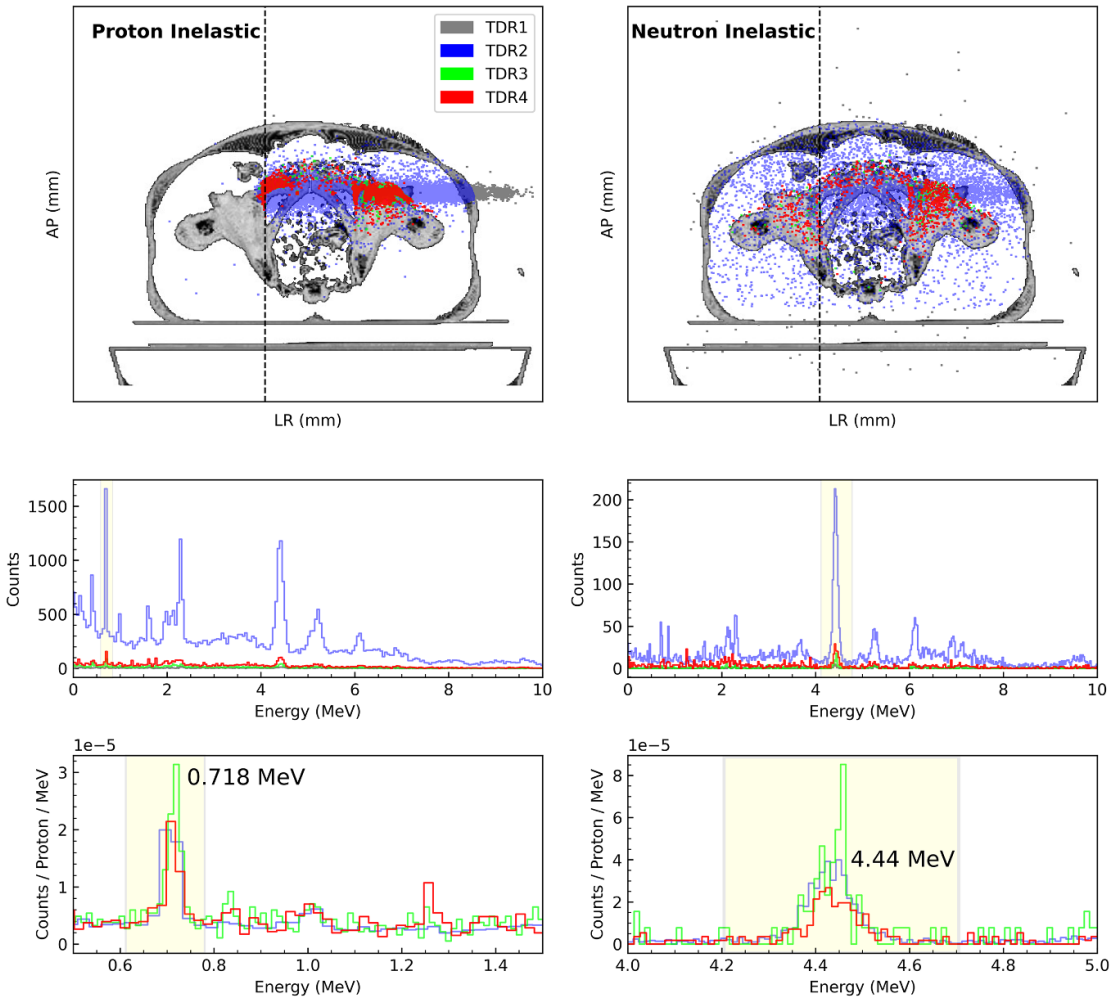

Figure 4. Illustration of PG emissions in a prostate patient from different tissue-dependent regions (TDR) for Spot-1 at a primary proton beam energy of 198.7 MeV. (Top) Spatial origins of PG signals, (middle) corresponding PG emission energies per MU, and (bottom) normalized PG spectra. The vertical dashed line in the top panel indicates the proton maximum dose depth (D_{max}) at 24.83 cm (refer to table 1: G4Engine). For further details, see the main text.

3.2. PG detection and imaging

In this section, we analyze PG detection using a two-stage, 64-pixelated PJ3-CC (see figure 2 for more details). For each PG signal interacting with the CC, the deposited energy and interaction positions in both Stage 1 and Stage 2 layers were recorded. Images were then reconstructed using the GPU-based KWBP algorithm. The detected PG signals were sorted to capture double-and-triple scattering events, which are key for accurate gamma imaging. Tables 1 and 2 provide a quantitative overview of PG signals emitted from the phantom and those detected by the CC for all clinically studied spots, including both the fixed energy layer set and the variable energy layer set delivered at the same MU but different spot positions. The PJ-MC package is designed to allow retrieval of double- and triple-scattering data, which is also quantitatively detailed in tables 1 and 2.

Figure 5 illustrates a clinical scenario involving proton beam energies of 198.7 MeV, delivering doses of 1.36, 18.99, and 19.45 MU at a gantry angle of 90°.

The top rows of figures 5 and 6 display the comparison of PG emission, detection, and reconstruction profiles in the patient phantom, each normalized to its respective maximum along the proton beam path. Figure 5 corresponds to the scenario with a fixed energy layer, while figure 6 represents the condition with a fixed MU and varying energy layers and spot positions. The subsequent 2D images illustrate the spatial origins of PG emissions within real patient anatomy, the detected gamma signals from all sources, and the reconstructed image generated by the KWBP algorithm based on signals captured by the Polaris CC positioned beneath the patient couch. The reconstructed PG images demonstrate the potential to visualize gamma hotspots along the beam path, supporting verification of proton range.

Previous work by Koide *et al* (2018) proposed improving gamma hotspot precision by filtering PG emissions at 4.44 MeV. Therefore, in this study, we extended this approach by applying an energy-gated

Table 1. Quantitative comparison of prompt gamma (PG) signals emitted and detected by the Polaris-J3 CC for three clinical scenarios (Spot 1, Spot 2, Spot 3) at 198.7 MeV proton energy. The table also presents the effects of applying a 4.44 MeV energy window on PG emission and detection. A comparision of proton maximum peak D_{max} is compared with the Raystation, and deduced PG ranges from PJ-MC are presented in the last.

Proton delivery and plan				
Location →	Spot 1	Spot 2	Spot 3	
Position X (cm)	3.49	3.49	3.49	
Position Y (cm)	14.26	1.04	−18.8	
Dose (MU)	1.36	19.05	18.97	
Protons ($\times 10^6$)	6.22	87.1	86.7	
Total PGs				
Emitted	1945 111	27 616 430	28 098 974	
Detected	8115	132 995	175 539	
Doubles	791	13 821	17 900	
Triples	414	7113	9062	
Energy gated (4.44 MeV)				
Emitted	179 015	2465 078	2534 630	
Detected	643	10 373	13 084	
Doubles	165	1153	1481	
Triples	80	568	721	
Proton range verification at 100% of peak value at D_{max}				
Location ↓	G4 Engine (cm)	RAYSTATION (cm)	KWBP (cm)	KWBP EG[a] (cm)
Spot1	24.83	24.56	22.73(↓2.10)	22.53(↓2.20)
Spot2	24.29	24.25	20.15(↓4.14)	21.36(↓2.93)
Spot3	24.69	24.28	19.19(↓5.50)	20.59(↓4.10)
Proton range verification at 80% of peak value at D_{max}				
Spot1	24.83	24.56	23.50(↓1.33)	23.62(↓1.21)
Spot2	24.29	24.25	22.20(↓2.09)	21.96(↓2.33)
Spot3	24.69	24.28	21.84(↓2.85)	23.82(↓0.87)
Proton range verification at 50% of peak value at D_{max}				
Spot1	24.83	24.56	25.38(↑0.55)	24.73(↓0.1)
Spot2	24.29	24.25	24.29(≈0.00)	24.79(↑0.5)
Spot3	24.69	24.28	25.23(↓0.54)	26.29(↑1.6)

[a] EG = 4.44 MeV PG Signal energy gated Window.

In parentheses → G4Engine—KWBP and/or G4Engine—KWBP EG[a]

↑ Increment by value (cm).

↓ Decrement by value (cm).

window across the entire PG data structure to understand its impact on the gamma hot spots and range verification. Tables 1 and 2 present the PG emission, detection, and range verification results based on reconstructed images using energy gating (EG) at 4.44 MeV. Figures 7 and 8 display the corresponding profile comparisons and 2D image results of PG emission, detection, and KWBP-based reconstruction under the energy-gated condition.

As can be seen in tables 1 and 2, around 90%–92% of emitted and detected PG signals were eliminated from the original spectra after EG. Nevertheless, KWBP algorithm still effectively reconstructed gamma hotspots, bringing their locations closer to the expected range compared to the unfiltered dataset with slightly distorted image for the spot 1 (figure 6, bottom panel), due to the low MU.

To further assess the impact of EG on PG range verification, the region corresponding to 50% of the maximum proton dose central peak was chosen as a reference point for evaluating PG signal distributions and associated uncertainties. This value typically aligns with a region of steep dose gradient, where the PG signal remains relatively stable and is particularly sensitive to small shifts in proton range near the D_{max} region. In contrast, the peak value at 100% may be affected by reconstruction artifacts or signal saturation,

Table 2. Quantitative comparison of prompt gamma (PG) signals emitted from the patient phantom and detected by the Polaris-J3 CC for clinical scenarios at 20 M.U. dose. The table also presents the effects of applying a 4.44 MeV energy window on PG emission and detection. A comparision of proton maximum peak D_{max} is compared with the Raystation, and deduced PG ranges from PJ-MC are presented in the last.

Proton delivery and plan				
Location →	Spot 4	Spot 5	Spot 6	
Energy (MeV)	182.2	173.8	157.6	
Position X (cm)	8.0	20.0	19.1	
Position Y (cm)	37.65	31.79	−5.16	
Protons ($\times 10^6$)	85.8	82.6	77.5	
Total PGs				
Emitted	6667 128	5986 857	18 307 806	
Detected	20 601	19 445	86 072	
Doubles	7531	7203	8741	
Triples	3956	3705	4467	
Energy gated (4.44 MeV)				
Emitted	605 136	550 630	1683 844	
Detected	1799	1735	6913	
Doubles	704	691	764	
Triples	369	332	408	
Proton range verification at 100% of peak value at D_{max}				
Location ↓	G4 Engine (cm)	RAYSTATION (cm)	KWBP (cm)	KWBP EG[a] (cm)
Spot4	20.33	20.43	16.25(↓4.08)	18.41(↓1.92)
Spot5	18.94	18.96	16.37(↓2.57)	17.88(↓1.06)
Spot6	15.86	15.86	15.69(↓0.17)	15.71(↓0.15)
Proton range verification at 80% of peak value at D_{max}				
Spot4	20.33	20.43	19.16(↓1.17)	21.02(↑0.69)
Spot5	18.94	18.96	18.87(↓0.07)	19.01(↑0.07)
Spot6	15.86	15.86	17.85(↑1.99)	17.48(↑1.62)
Proton range verification at 50% of peak value at D_{max}				
Spot4	20.33	20.43	21.74(↑1.41)	23.09(↑2.76)
Spot5	18.94	18.96	21.56(↑2.62)	22.05(↑3.11)
Spot6	15.86	15.86	20.78(↑4.92)	19.40(↑3.54)

[a] EG = 4.44 MeV PG Signal energy gated Window.

In parentheses → G4Engine—KWBP and/or G4Engine—KWBP EG[a]

↑ Increment by value (cm).

↓ Decrement by value (cm).

while the distal tail of the distribution can be noisy and less reliable. Therefore, using the 50% point helps balance sensitivity and signal stability, reducing uncertainty in range estimation and allowing for more consistent comparisons across datasets. Tables 1 and 2 present the PG range values and their associated uncertainties for both non-gated and EG conditions. The results indicate a substantial improvement in range accuracy with EG, albeit at the cost of reduced PG signal detection. These improvements highlight the robustness of our approach in enhancing PG imaging for proton therapy range verification.

4. Discussions

In this study, a clinical simulation package, PJ-MC, was developed to simulate the origins of PG emissions and their detection by the PJ3 CC and image reconstruction within the patient?s anatomy during proton therapy. The workflow for emission, detection, and imaging of PG signals is outlined in figure 1, beginning with the import of CT images of a prostate cancer patient using DCMTK software. These CT images were converted into a voxelized simulation model using Geant4's DICOM libraries, following Schneider?s approach, which divides the HU scale (−1000 to 1600) into 24 material groups based on elemental

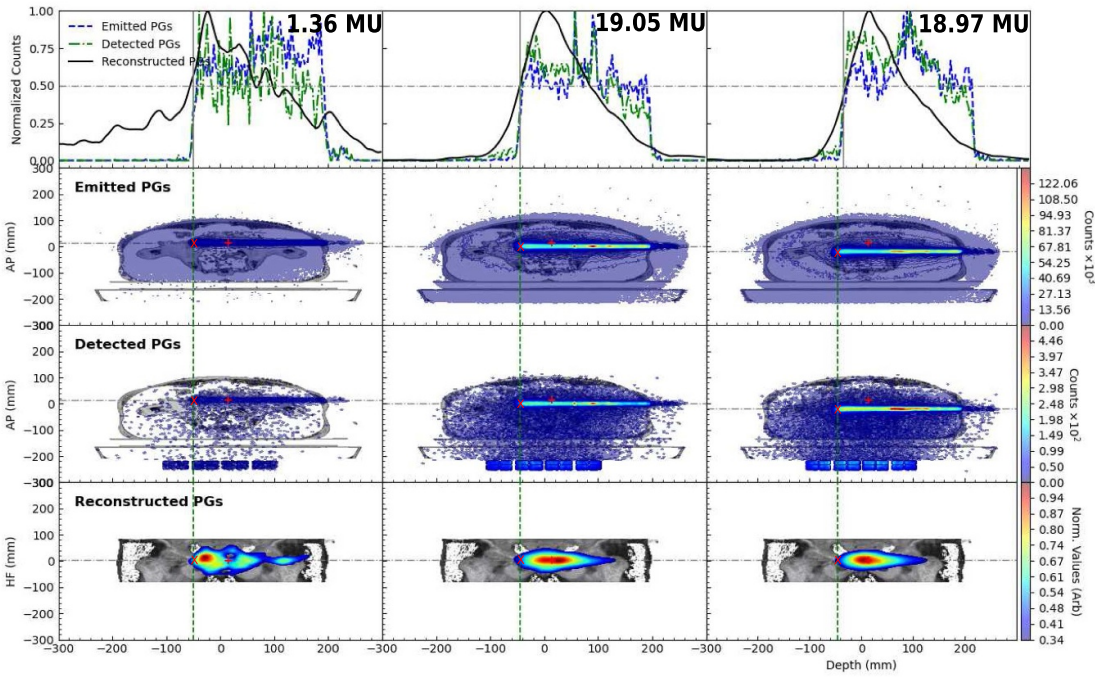

Figure 5. A comprehensive presentation of delivery of three clinical beam spots at location 'X' at fixed energy layer ≈198.7 MeV. (Top) linear profiles comparison, (Bottom) are the emission of PGs, detection of PGs and reconstruction of PGs using KWBP algorithm. Vertical dash line is the proton Maximum (D_{max} and '+' refers isocenter. For more details see text.

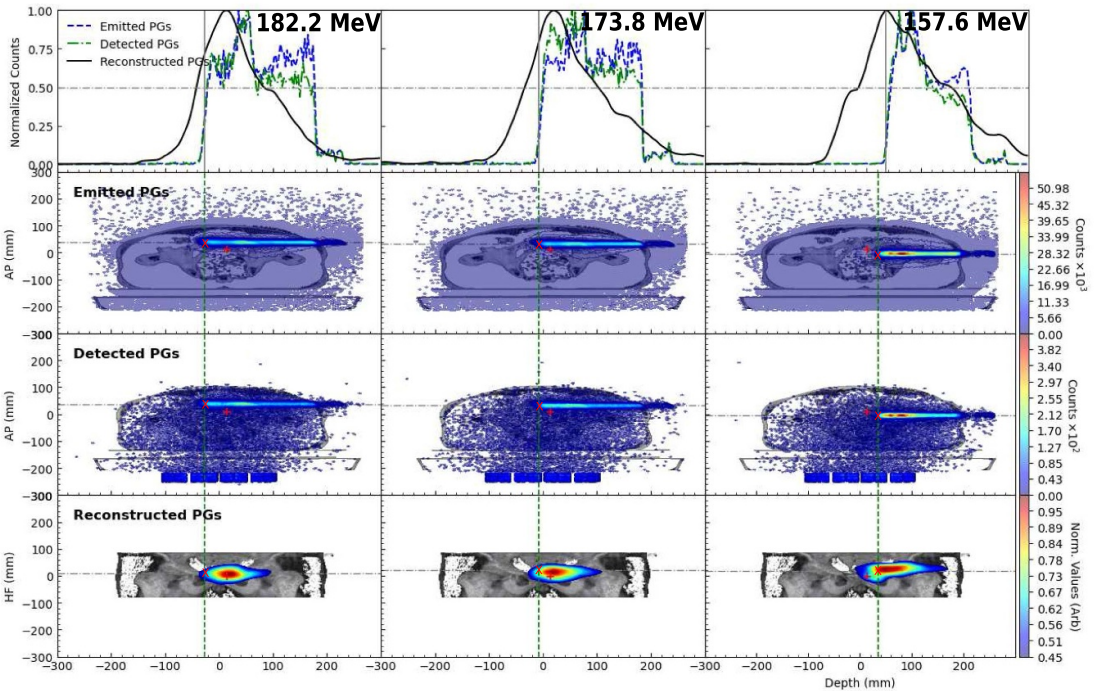

Figure 6. A comprehensive presentation of delivery of three clinical beam spots at location 'X' at different locations with a fixed MU (i.e. 20 M.U.) and varying energy layers. (Top) linear profiles comparison, (Bottom) the emission of PGs, detection of PGs, and reconstruction of PGs using the KWBP algorithm. The vertical dashed line indicates the proton maximum dose depth (D_{max}), and the '+' symbol marks the isocenter. For more details, see text.

composition and mass density. This method ensures an accurate representation of tissue properties, allowing for more realistic simulations. It may be mentioned that, while PJ-MC is capable of resolving small inter-spot distances at the simulation level, the KWBP reconstruction of PG hotspots can exhibit and uncertainty of ±1 to ±2 cm due to limited-angle camera distortion, which can further be reduced through post-processing techniques (Jiang *et al* 2023).

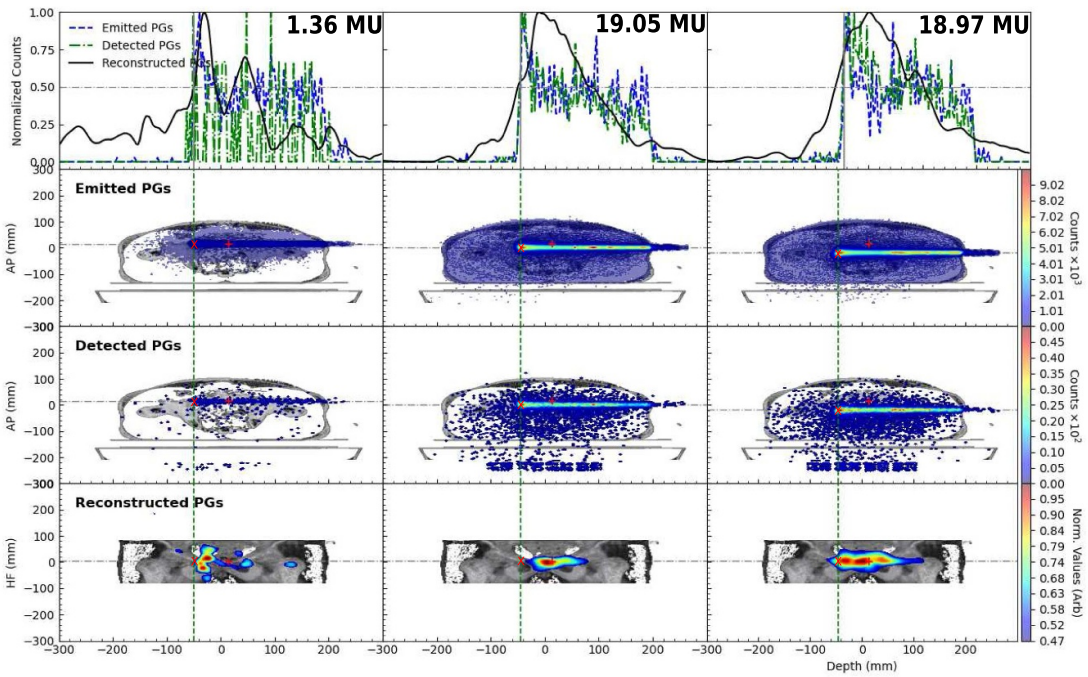

Figure 7. An energy gated (EG) comprehensive presentation of delivery of three clinical beam spots at location 'X' at fixed energy layer ≈198.7 MeV. (Top) linear profiles comparison, (Bottom) are the emission of PGs, detection of PGs and reconstruction of PGs using KWBP algorithm. Vertical dash line is the proton Maximum (D_{max} and '+' refers isocenter. For more details see text.

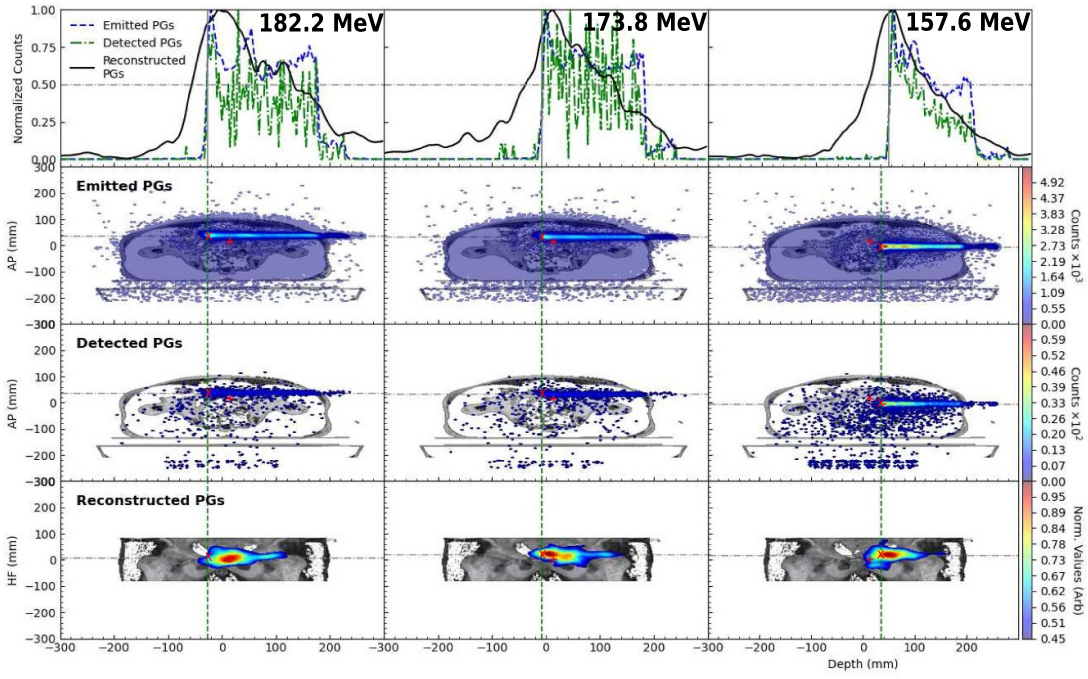

Figure 8. An energy gated (EG) comprehensive presentation of delivery of three clinical beam spots at location 'X' at different locations with a fixed MU (i.e. 20 M.U.) and varying energy layers. (Top) linear profiles comparison, (Bottom) are the emission of PGs, detection of PGs and reconstruction of PGs using KWBP algorithm. Vertical dash line is the proton Maximum (D_{max} and '+' refers isocenter. For more details see text.

To closely match actual treatment conditions, the PPB parameters were tuned using commissioning data, and the proton ranges from the G4-Engine were validated in frame of Raystation MC at three clinical treatment spots, as presented in tables 1 and 2. The experimental setup was designed to assess the feasibility of mounting a detection system beneath the patient couch, as shown in figure 2. A two-stage detector system composed of 64 pixelated CZT crystals is used to monitor PG emissions during proton therapy. Stage 1

consists of 32 CZT crystals, each measuring 2 cm ? 1 cm ? 2 cm, while Stage 2 contains thicker CZT crystals measuring 2 cm ? 1.5 cm ? 2 cm. The detector records the total number of PGs emitted from the phantom during irradiation. The simulation included the delivery of three clinical beam spots, each with a fixed X position but varying Y positions, using a single energy layer of 198.7 MeV with protons delivered at a 90° gantry angle.

The analysis of proton-induced PG emissions revealed distinct energy peaks and an exponentially decaying continuum, primarily resulting from carbon and oxygen interactions (figure 3). A comparison of total PG emissions, proton-induced PG spectra, and neutron-induced PG spectra indicates that neutron interactions contribute significantly to the PG spectrum, though at a lower intensity, approximately one order of magnitude weaker than proton-induced PG emissions.

The classification of tissues into four TDR1-TDR4 highlights the influence of elemental composition in patient anatomy on PG production, as shown in figure 4. From an elemental composition perspective, this classification provides valuable insight into how different tissues contribute to PG emissions. For example, the characteristic 4.44 MeV gamma emission predominantly arises from carbon de-excitation ($^{12}C^{*}$), making it a key marker for soft tissues. But as presented in figure 3, the neutron cross section contribution in populating the excited $^{12}C^{*}$ state appears to contribute around 27%. Involvement of denser tissues in the prostrate region may generate additional gamma lines such as from Calcium or Magnesium reactions provided proton traverse in this tissue region. Figure 4(top and middle panel) illustrates that TDR2 exhibits the highest PG emission intensity. This is consistent with the beam's traversal pattern, as the majority of protons pass through TDR2, resulting in increased interaction volume and, therefore, higher gamma production. The elevated emissions observed are thus primarily attributed to the greater number of voxels intersected by the beam path within this region. However, it is also important to consider the contribution of secondary particles?particularly neutrons?which follow a similar, though more scattered, trajectory. These secondary neutrons induce additional gamma emissions via inelastic nuclear interactions, contributing further to the overall spectral profile in TDR2 and surrounding regions. This suggests that both geometric path length and particle interaction dynamics influence the observed PG spectra. The zoomed-in panel in figure 4(bottom panel) focuses on the normalized PG energy spectra from different TDRs. Classifying PG signals may be valuable not only for imaging purposes but also from a fundamental physics point of view, since different nuclear reactions produce gamma rays at specific energies, each associated with interactions involving particular elements. To enable meaningful comparisons, the spectra were normalized by energy bin and the number of primary incident protons. As can be seen, a relatively lower intensity of the 0.718 MeV gamma line associated with proton-induced reactions populated in TDR2 compared to other regions of tissues. This reduction may be linked to a higher oxygen concentration in that region, as supported by previous experimental studies (Martins *et al* 2020). Importantly, the 0.718 MeV gamma line is known to originate from interactions involving residual carbon contamination in the classified region, suggesting that its relative intensity may serve as an indicator of elemental composition.

Conversely, when analyzing gamma rays resulting from neutron inelastic scattering, TDR4 contributed the least to the final neutron-induced PG spectrum (see also figure 3). This may suggest that the probability of specific reactions-such as neutron-induced excitation and de-excitation of ^{12}C nuclei-varies depending on the energy of secondary neutrons interactions by the tissue elements, and its composition. In the present work, TDRs represent a heterogeneous region of tissues because of HU-derived material properties from patient CT data, therefore, assigning specific material indices may improve the accuracy of PG-based elemental analysis. Earlier work (Olsson *et al* 1989, Martins *et al* 2020) has shown the feasibility of using homogeneous phantoms to identify elemental signatures, such as those from oxygen and carbon. The 2D histogram in figure 4 clearly indicates that PG signals from neutron induced reactions leads to noise (extended tails) in the CC. Similar tail regions in both the ground truth and detection space were characterized as resulting from secondary neutron-induced reactions, as reported by Zarifi *et al* (2017), which is consistent with our findings. As such, neutrons scattering results in PG emissions originating from farther positions along the beam path, particularly in lower-density tissues (TDR1-TDR2). Such behavior suggests that neutron-induced emissions may include artifacts in image reconstruction.

This study is designed to record all PG signals in the PJ3 CC from the patient anatomy and to classify doubles- and triples-Compton scattering events for PG image reconstruction. Tables 1 and 2 summarizes the PG signals emitted and detected at studied clinical cases for six spots at wide variety of energies, MUs and positions, showing clear variations due to patient anatomy and beam positioning. Furthermore, the response time of the Polaris CC was approximated using an event-by-event rate matching the conditions described in our previous work (Maggi *et al* 2020), where the timing behavior of the CZT detectors was experimentally studied. Although the intrinsic properties of the CZT crystals (e.g. charge transport, trapping effects) were not explicitly modeled in this simulation, the applied timing structure mimics the low-dose-rate operational regime and temporal characteristics observed in real detectors. This approximation introduces a limited and

acceptable gap between the simulated and real detector response, particularly given the focus on imaging trends rather than absolute count rates.

Figures 5 and 6 show the PG emission, detection, and reconstruction for non-gated conditions, while figures 7 and 8 present the same for EG conditions using the 4.44 MeV photon window. In the non-gated case, the linear depth profiles show a close match between emitted and detected PGs for all beam spots. As can be seen, the 2D histograms shows PGs are emitted in all directions with counts on the order of 10^7, whereas the detector PJ3-CC records around 10^4 counts, leading to smooth and well-localized reconstructed PG hotspots. In the gated case, although the 4.44 MeV selection improves energy specificity, the total number of emitted and detected PGs is significantly reduced. This further lower signal level results in noisy detection profiles and less stable reconstructions, as can be seen by the irregular shapes and additional artifacts in the bottom row of figures 7 and 8. The corresponding quantitative values from figures 5–8 are summarized in tables 1 and 2. As can be seen in tables 1 and 2 (data illustrated in figures 5 and 6), approximately 0.3% to 0.6% of PG signals were detected for the studied spots. This variation may be influenced by the experimental configuration, including the placement of the CC beneath the treatment couch, as well as differences in beam energy and MU across the spots. Furthermore, approximately 10% of the detected PG signals go through double scattering, while only ≈5% of the total PGs were triple scattered. Koide *et al* (2018) proposed that using an energy-gated window centered around 4.44 MeV is beneficial for improving the localization of gamma hotspots by selectively filtering PG emissions. We observed, when applying an energy-gated window, the overall PG emission rate was reduced to ≈9% of the total spectrum, with a significant decrease in detected PG signals, dropping to just ≈8% of the original count. The qualitative values obtained after energy filtering are presented in tables 1 and 2, while figures 7 and 8 illustrates how this method slightly improves hotspot reconstruction. Although EG reduces PG signal availability, the KWBP algorithm still effectively enhances gamma hotspot localization, resulting in a closer match to expected ranges compared to unfiltered data (figures 7 and 8, bottom panel). The application of energy-gated filtering at 4.44 MeV slightly improves hotspot localization, but this comes at the cost of signal reduction, particularly in low-dose cases and they may not be accurate everytime for localization of depth dose positions. As can be seen in figure 7, corresponding to 1.36 MU, the reconstructed PG profile (solid black line) exhibits fluctuations and a less sharp fall-off, which is primarily due to poor statistical quality of the PG data. This results in increased noise and less accurate backprojection, producing the ripples and extended tail in the reconstruction. However, as the MU increases, the statistical quality improves significantly and thus reflects a smoother reconstructed profiles with a well-defined fall-off and minimal tailing.

To evaluate the overall performance of PG-based range verification, a Mean absolute percentage error (MAPE) analysis was conducted across six clinical beam spots at both 100% and 50% of the maximum peak value of the D_{max}. At the 100% peak value of the D_{max}, the KWBP method yielded a MAPE of ≈15%, while the energy-gated version showed a reduced MAPE of ≈8%, indicating improved accuracy through selective energy filtering. However, considering higher signal stability at 50% of the peak value at D_{max}, we observed the non-gated KWBP method achieved a lower MAPE of ≈8%, outperforming the gated approach at ≈10%.

Hsi *et al* (2009) reported that range definitions in proton therapy are often based on 80% of the D_{max} (Bragg peak). Accordingly, we evaluated the MAPE at 80% of the D_{max}. We observed a MAPE of ≈7% and ≈5% for non-gated and gated PGs, respectively, showing a slight improvement (≈1%) compared to the values at 50% of the D_{max}.

These results suggest that while EG can slightly improve range accuracy at studied peak value of D_{max} by filtering out background signals, it may also introduce additional noise and reconstruction artifacts due to reduced photon counts, ultimately lowering localization precision in otherwise stable regions. On the other hand, 50% and 80% D_{max} region may thus considered as a reference point for PG-based range verification due to an assumption on balancing signal strength and stability. It may be mentioned that the energy gated technique not improve always the localization of proton depth dose due to significant signal loss and may not be used for PG-based proton range verification from PJ3-CC.

The finding of the present work demonstrate the impact of patient anatomy on range verification based on PG imaging. The results indicate that variations in tissue composition can shift gamma hotspots, influencing PG-based range verification. The PJ-MC package provides a robust platform for investigating secondary gamma interactions and evaluating the tissue-dependent variations in PG emissions. Future studies should focus on optimizing energy-gated techniques to maximize signal retention while maintaining imaging accuracy, particularly in low-dose treatment scenarios. Expanding the current work to multiple energy layers and performing clinical validation in patient-specific studies will further enhance the clinical applicability of PG imaging for proton therapy verification.

5. Conclusion

This study aimed to develop a MC simulation package, PJ-MC, to model the entire PG imaging process, including PG emission, detection, and image reconstruction, within patient anatomy for proton therapy verification using the PJ3 CC. The simulation framework provides a valuable tool for investigating PG signal behavior in clinically relevant conditions, enabling a better understanding of PG imaging performance and its optimization for dose verification. Proton-induced PG emissions were found to be the dominant source of PG signals, with neutron-induced emissions contributing at a lower intensity (approximately one order of magnitude lower). The classification of tissues into four density regions (TDR1-TDR4) revealed significant anatomical influences on PG emissions, particularly highlighting the contribution of bone (TDR4) and soft tissue (TDR2) interactions in shaping PG spectra. The energy-gated filtering at 4.44 MeV reducing spectral contamination from scattered emissions, though at the cost of a reduced signal count (≈90% to 95% of the total PG emissions loss) and affects reconstruction of gamma hot spots for low doses. Further, PG-based range verification was assessed using MAPE analysis at 100% and 50% of the peak value of maximum proton range (D_{max}). While EG slightly improved accuracy at 100% of D_{max} by reducing MAPE from ≈15% to ≈7%–8%), the 80%–50% of peak value at D_{max} region showed greater stability, with the non-gated method achieving a lower MAPE (≈8%) than the gated approach (≈10%). These results suggest that 80% and 50% peak value at D_{max} can be a greater choice for PG-based range verification, and that EG may not always enhance localization due to reduced photon statistics. The findings of this study highlight the critical role of patient anatomy and tissue composition in PG-based range verification, as slight shifts in gamma hotspots appear due to prominent PG signals from denser regions during proton traversal. The PJ-MC package provides a robust platform for evaluating PG emissions and secondary gamma interactions in a clinically relevant setting. We plan to extend this study to multiple energy layers at two gantry angles to provide comprehensive results on gamma imaging and its applicability in proton therapy verification.

Data availability statement

The data that support the findings of this study will be openly available following an embargo at the following URL/DOI: https://drive.google.com/drive/folders/1rRFZ6HQY4CEM2dSwcg3b0wIB2FEqsV30?usp=sharing.

Acknowledgments

V R S, J C P, L R acknowledge the support from National Institutes of Health under Grants No. R01-CA279013 and R01-EB032680. The simulated data used in this work was generated using the UMBC High Performance Computing Facility (hpcf.umbc.edu) and the financial contributions from NIH, NSF, CIRC, and UMBC. All authors declare that they have no known conflicts of interest in terms of competing financial interests or personal relationships that could have an influence or are relevant to the work reported in this paper.

Conflict of interest

The authors declare that there are no conflicts of interest related to this work.

ORCID iDs

V R Sharma https://orcid.org/0000-0002-4254-5653
M K Gobbert https://orcid.org/0000-0003-1745-2292
L Ren https://orcid.org/0009-0005-2384-5676

References

Agostinelli S *et al* 2003 Geant4-a simulation toolkit *Nucl. Instrum. Methods Phys. Res. A* **506** 250–303
Allison J *et al* 2006 Geant4 developments and applications *IEEE Trans. Nucl. Sci.* **53** 270–8
Allison J *et al* 2016 Recent developments in geant4 *Nucl. Instrum. Methods Phys. Res. A* **835** 186–225
Berthold J *et al* 2021 First-in-human validation of CT-based proton range prediction using prompt gamma imaging in prostate cancer treatments *Int. J. Radiat. Oncol. Biol. Phys.* **111** 1033–43
Bom V, Joulaeizadeh L and Beekman F 2011 Real-time prompt gamma monitoring in spot-scanning proton therapy using imaging through a knife-edge-shaped slit *Phys. Med. Biol.* **57** 297–308
Brun R and Rademakers F 1997 Root - an object oriented data analysis framework *Nucl. Instrum. Methods Phys. Res. A* **389** 81–86
Chen H, Chen-Mayer H H, Turkoglu D J, Riley B K, Draeger E and Polf J P 2018 Spectroscopic compton imaging of prompt gamma emission at the mev energy range *J. Radioanal. Nucl. Chem.* **318** 241–6

Fontana M, Ley J-L, Dauvergne D, Freud N, Krimmer J, Letang J M, Maxim V, Richard M-H, Rinaldi I and Testa E 2020 Monitoring ion beam therapy with a compton camera: simulation studies of the clinical feasibility *IEEE Trans. Radiat. Plasma Med. Sci.* **4** 218–32
Hsi W C *et al* 2009 Energy spectrum control for modulated proton beams *Med. Phys.* **36** 2297–308
Hu M, Jiang L, Cui X, Zhang J and Yu. J 2018 Proton beam therapy for cancer in the era of precision medicine *J. Hematol. Oncol.* **11** 136
Hueso-González F, Rabe M, Ruggieri T A, Bortfeld T and Verburg J M 2018 A full-scale clinical prototype for proton range verification using prompt gamma-ray spectroscopy *Phys. Med. Biol.* **63** 185019
Jacquet M *et al* 2021 A time-of-flight-based reconstruction for real-time prompt-gamma imaging in proton therapy *Phys. Med. Biol.* **66** 135003
Janson M, Glimelius L, Fredriksson A, Traneus E and Engwall E 2024 Treatment planning of scanned proton beams in raystation *Med. Dosimetry* **49** 2–12
Jeyasugiththan J and Peterson S W 2015 Evaluation of proton inelastic reaction models in geant4 for prompt gamma production during proton radiotherapy *Phys. Med. Biol.* **60** 7617–35
Jiang Z, Polf J C, Barajas C A, Gobbert M K and Ren L 2023 A feasibility study of enhanced prompt gamma imaging for range verification in proton therapy using deep learning *Phys. Med. Biol.* **68** 075001
Koide A *et al* 2018 Precision imaging of 4.4 MeV gamma rays using a 3-D position sensitive compton camera *Sci. Rep.* **8** 8116
Krimmer J, Dauvergne D, Létang J M and Testa E 2018 Prompt-gamma monitoring in hadrontherapy: a review *Nucl. Instrum. Methods Phys. Res. A* **878** 58–73
Lomax A J 2019 Myths and realities of range uncertainty *Br. J. Radiol.* **93** 1107
Maggi P, Peterson S, Panthi R, Mackin D, Yang H, He Z, Beddar S and Polf J 2020 Computational model for detector timing effects in Compton-camera based prompt-gamma imaging for proton radiotherapy *Phys. Med. Biol.* **65** 125004
Martins P M, Bello R D, Ackermann B, Brons S, Hermann G, Kihm T and Seco J 2020 Pibs: Proton and ion beam spectroscopy for *in vivo* measurements of oxygen, carbon and calcium concentrations in the human body *Sci. Rep.* **10** 7007
Martins P M, Draeger E and Wrońska A 2024 Editorial: prompt-gamma imaging in particle therapy *Front. Phys.* **12** 1331047
Moteabbed M, España S and Paganetti H 2011 Monte carlo patient study on the comparison of prompt gamma and pet imaging for range verification in proton therapy *Phys. Med. Biol.* **56** 1063–82
Nishioka K *et al* 2022 A single-institution prospective study to evaluate the safety and efficacy of real-time-image gated spot-scanning proton therapy (RGPT) for prostate cancer *Int. J. Radiat. Oncol. Biol. Phys.* **114** e235
Olsson N, Trostell B and Ramstrom E 1989 Cross sections and partial kerma factors for elastic and inelastic neutron scattering from carbon in the energy range 16.5–22.0 MeV *Phys. Med. Biol.* **34** 909–26
Paganetti H 2012 Range uncertainties in proton therapy and the role of Monte Carlo simulations *Phys. Med. Biol.* **57** R99–R117
Panthi R, Maggi P, Peterson S, Mackin D, Polf J and Beddar S 2021 Secondary particle interactions in a compton camera designed for *in vivo* range verification of proton therapy *IEEE Trans. Radiat. Plasma Med. Sci.* **5** 383–91
Parodi K and Polf J C 2018 *In vivo* range verification in particle therapy *Med. Phys.* **45** e1036–50
Polf J C, Panthi R, Mackin D S, McCleskey M, Saastamoinen A, Roeder B T and Beddar S 2013 Measurement of characteristic prompt gamma rays emitted from oxygen and carbon in tissue-equivalent samples during proton beam irradiation *Phys. Med. Biol.* **58** 5821–31
Reaz F, Sjobak K N, Malinen E, Edin N F J and Adli E 2022 Sharp dose profiles for high precision proton therapy using strongly focused proton beams *Sci. Rep.* **12** 18919
Richter C *et al* 2016 First clinical application of a prompt gamma based *in vivo* proton range verification system *Radiother. Oncol.* **118** 232–7
Schneider W, Bortfeld T and Schlegel W 2000 Correlation between ct numbers and tissue parameters needed for monte carlo simulations of clinical dose distributions *Phys. Med. Biol.* **45** 459–78
Wang J-L *et al* 2022 Prompt gamma spectroscopy retrieval algorithm for element and density measurements accelerated by cloud computing *Front. Phys.* **10** 961162
Wrońska A *et al* 2021 Prompt-gamma emission in geant4 revisited and confronted with experiment *Phys. Med.* **88** 250–61
Yap J S L, Bal N J S, Kacperek A, López J R and Welsch C P 2021 Medipix3 for dosimetry and real-time beam monitoring: first tests at a 60 MeV proton therapy facility *J. Instrum.* **16** T11001
Zarifi M, Guatelli S, Bolst D, Hutton B, Rosenfeld A and Yujin Q 2017 Characterization of prompt gamma-ray emission with respect to the bragg peak for proton beam range verification: a Monte Carlo study *Phys. Medica* **33** 197–206